# Correlated polarization switching in the proximity of a 180° domain wall

Vasudeva Rao Aravind,[1,2] A. N. Morozovska,[3] Saswata Bhattacharyya,[1] D. Lee (이동화),[4] S. Jesse,[5] I. Grinberg,[6] Y. L. Li,[7] S. Choudhury,[1] P. Wu,[1] K. Seal,[5] A. M. Rappe,[6] S. V. Svechnikov,[3] E. A. Eliseev,[8] S. R. Phillpot,[4] L. Q. Chen,[1] Venkatraman Gopalan,[1,*] and S. V. Kalinin[5,†]

[1]*Materials Research Institute and Department of Materials Science and Engineering, Pennsylvania State University, University Park, Pennsylvania 16802, USA*

[2]*Physics Department, Clarion University of Pennsylvania, Clarion, Pennsylvania 16214, USA*

[3]*V. Lashkarev Institute of Semiconductor Physics, National Academy of Science of Ukraine, 41, pr. Nauki, 03028 Kiev, Ukraine*

[4]*Department of Materials Science and Engineering, University of Florida, Gainesville, Florida 32611, USA*

[5]*Center for Nanophase Materials Sciences, Oak Ridge National Laboratory, Oak Ridge, Tennessee 37831, USA*

[6]*Department of Chemistry, University of Pennsylvania, Philadelphia, Pennsylvania, 19104 USA*

[7]*Pacific Northwest National Laboratory, Richland, Washington 99352, USA*

[8]*Institute for Problems of Materials Science, National Academy of Science of Ukraine, 3, Krjijanovskogo, 03142 Kiev, Ukraine*

(Received 6 April 2010; revised manuscript received 5 June 2010; published 27 July 2010)

Domain-wall dynamics in ferroic materials underpins functionality of data storage and information technology devices. Using localized electric field of a scanning probe microscopy tip, we experimentally demonstrate a surprisingly rich range of polarization reversal behaviors in the vicinity of the initially flat 180° ferroelectric domain wall. The nucleation bias is found to increase by an order of magnitude from a two-dimensional (2D) nucleus at the wall to three-dimensional nucleus in the bulk. The wall is thus significantly ferroelectrically softer than the bulk. The wall profoundly affects switching on length scales on the order of micrometers. The mechanism of correlated switching is analyzed using analytical theory and phase-field modeling. The long-range effect is ascribed to wall bending under the influence of a tip with bias that is well below the bulk nucleation level at large distances from the wall. These studies provide an experimental link between the macroscopic and mesoscopic physics of domain walls in ferroelectrics and atomistic models of 2D nucleation.

DOI: 10.1103/PhysRevB.82.024111 PACS number(s): 77.80.Dj, 68.37.−d, 77.80.Fm, 77.84.Ek

## I. INTRODUCTION

Dynamics of interfaces and their interaction with microstructure and defects is the key element determining functionality of ferroelectric and ferromagnetic materials,[1] electrochemical systems,[2–4] and phase transformations.[5] Interface dynamics controls the switching speed, critical bias, and retention in ferroic[6] and phase change memories, energy storage density in batteries and capacitors, and microstructure and properties of materials.[7] This recognition of the role of interface behavior in materials science and energy and information technologies has stimulated an intensive effort on understanding the relationship between electronic, atomic, and mesoscopic structures and dynamic behavior of the interface.

Domain-walls separating regions with opposite ferroelectric polarization are the prototypical example of interfaces in ferroic materials and have been extensively studied over the last 60 years.[8] The narrow width of the 180° wall necessitates the formation of the two-dimensional (2D) nuclei as a rate-limiting step in wall motion and results in strong lattice and defect pinning.[9] Notably, similar motion mechanisms operate at phase transformation and solid-state reaction fronts and other high-energy interfaces. On the mesoscopic scale, wall-defect interactions give rise to a rich spectrum of dynamic behaviors[1,10] reflected in the complex self-affine wall geometries observed down to ~10–30 nm length scales.[11,12]

The synergy between electron and scanning probe microscopies has allowed comprehensive understanding of the *static* domain-wall structures at atomic and mesoscopic scales.[13–15] Switching of ferroelectric domains generated in the two limits of extremely large fields applied far away from the domain wall (i.e., bulk switching through nucleation) or smaller fields applied at the domain wall (i.e., field-induced domain-wall motion) have been investigated in previous work and are likewise now well understood.[1] In the intermediate region, a number of observations,[16–18] including the correlated nucleation at the moving domain-wall front,[19,20] suggest that the walls can strongly affect the properties of adjacent material due to long-range electrostatic and elastic fields. Nevertheless, fundamental questions, such as whether the nucleation energy of a 2D nucleus[21] on the wall can be measured directly, and especially the effect of the wall on the nucleation in the vicinity of the wall[22] have never been answered experimentally.

Here, we report on experimental studies of the nucleation behavior of ferroelectric domains using the spatially localized electric field of a biased scanning probe microscopy (SPM) tip. This allows us to directly measure the intrinsic critical voltage for the formation of 2D nucleus at the wall[23,24] as well as to reveal the influence of the wall on the nucleation in the bulk. Surprisingly, we find that nuclei formed in the bulk interact with the domain wall even at extremely large micron-scale range, significantly lowering the barriers for domain nucleation. These finding have obvious implications for dynamics of polycrystalline ferroelectrics, and similar mechanisms can be operational in other systems with high-energy interfaces, including electrochemical systems and solid-solid transformations.

 

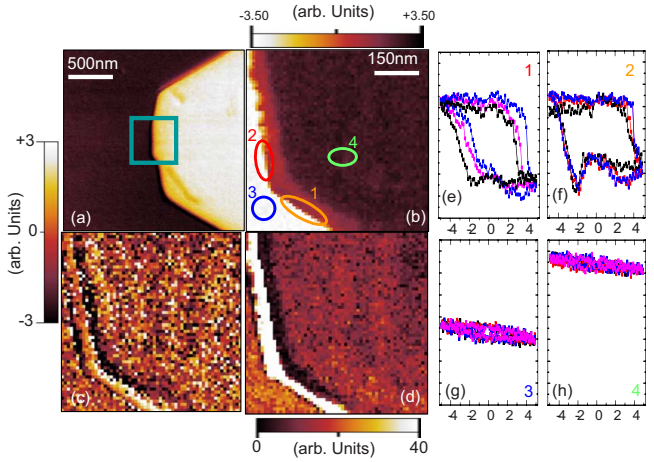


FIG. 1. (Color online) (a) Mixed piezoresponse force microscopy images of the domain structure before and the SS-PFM scan with ±5.0 V voltage window. Panels (b), (c) and (d) represent area under the central square in (a). Note that while domain wall moved during the experiment, the high veracity of SS-PFM map indicates that no significant wall rearrangement was happening during single pixel or scan line acquisition. (b) The piezoresponse, (c) imprint and (d) work of switching SS-PFM map in the domain wall region. [(e)–(h)] Hysteresis loops from selected locations.

## II. SWITCHING SPECTROSCOPY PFM OF A FERROELECTRIC WALL

Here we study local dynamic behavior of ferroelectric domain wall using spatially localized electric field of a biased scanning probe microscopy tip. The application of the local field to the wall results in the local wall displacement and associated change in electromechanical response of the surface is detected as piezoresponse force microscopy (PFM) signal. This approach allows probing intrinsic (as opposed to extended defect-controlled) polarization dynamics since the number of defects within the probing volume is necessarily small. The spatial extent and strength of the electric field acting on the wall can be controlled in a broad range by varying tip-wall separation and tip bias.

Near stoichiometric (NS) crystal of $z$-cut lithium niobate (LN), 900 nm thick was used for this study. Indium tin oxide (ITO) electrode was deposited on a $+z$ surface by magnetron sputtering to establish the bottom electrode. The NSLN sample was mounted with its $-z$ surface upward on the 0.5-mm-thick congruent lithium niobate substrate using organic adhesive. Conductive silver paste was used to establish electrical contact with the bottom ITO electrode. To create the ferroelectric domain wall, the polarization in LN single crystal was reversed by the application of a high (44–66 V) bias pulse to the SPM tip, resulting in a macroscopic (~2 $\mu$m) domain of a characteristic hexagonal shape as shown in Fig. 1(a). The effective tip radius was calibrated from the observed wall width and the bulk nucleation potential, as described in Sec. III A

To address nanoscale polarization switching dynamics in the presence of domain wall, we utilize switching spectroscopy PFM (SS-PFM).[25] SS-PFM is implemented on a commercial SPM system (Asylum MFP-3D) equipped with external data-acquisition electronics based on NI-6115 fast DAQ card to generate the probing signal and store local hysteresis loops and correlate them with surface topography.[25] In SS-PFM, the tip approaches the surface of the sample vertically, with the deflection signal being used as the feedback, until the deflection set point is achieved. Once the tip-surface contact at the predefined indentation force is established, the piezomotion is stopped and a hysteresis loop is acquired. During the acquisition of a hysteresis loop in SS-PFM, the tip is fixed at a given location on the surface of the sample and the wave form $V_{tip}=V_{dc}+V_{ac}\cos\omega t$ is applied to the tip. Here, $V_{ac}$ is the amplitude of the PFM driving signal and the corresponding frequency is typically in the 200–500 kHz range. The probing signal $V_{dc}$ is the dc bias applied to the tip formed by the triangular wave (0.1–1 Hz) modulated by square wave (~100 Hz) to yield on-field and off-field responses.[25] Application of sufficiently high dc bias results in the nucleation and subsequent growth of domains of opposite polarity below the tip with a concurrent change of the PFM signal from $PR$ (initial state) to $-PR$ (switched state). The resulting $PR$ dependence of dc bias contains information on polarization dynamics, including wall motion, domain nucleation and growth below the tip. In SS-PFM, the hysteresis loops are acquired at each point in an $M\times N$ grid that is further analyzed to yield 2D maps of polarization switching parameters such as work of switching, imprint, coercive and nucleation biases, etc.

Here, the local electromechanical hysteresis loops are acquired over densely spaced (10 nm) grid of points (60 $\times$60 pixels) and analyzed to produce 2D maps of switching parameters. To ensure the reversibility of tip-induced wall displacement, the PFM images were acquired before and after the SS-PFM mapping. While the domain wall shifts on average, the length traveled (~1 pixel per line scan in the image and ~30 pixels total per image) is small compared to the total number of measurement points (3600). Thus, the wall dynamics is almost reversible. The measurements are performed as a function of bias window (i.e., maximal bias during the hysteresis loop acquisition) to decouple the bias and distance effects on wall dynamics. The scan size was adjusted for large bias windows.

The three-dimensional (3D) data sets and 2D SS-PFM maps contain the information on the domain nucleation in the presence of the wall. The averaged piezoelectric response image in Fig. 1(b) shows dark and bright regions with no switching (that correspond to the original domains) and the region of intermediate contrast. The examination of the hysteresis loops illustrates that the loops are closed in the bright and dark regions and are open in the region of intermediate contrast. The bright regions in Fig. 1(d) shows that in the vicinity of the domain wall the work of switching (WoS) (i.e., area under the loop) is nonzero and the hysteresis loops are open even below the threshold bias for bulk nucleation. The bright region is quite large, indicating that the presence of the domain wall has a strong influence on polarization dynamics even at relatively long ranges.

Analysis of the SS-PFM data as a function of bias window (the maximum amplitude of dc bias applied to the probe) quantifies the dependence of the switching behavior as a function of probe from the domain wall. The dynamic

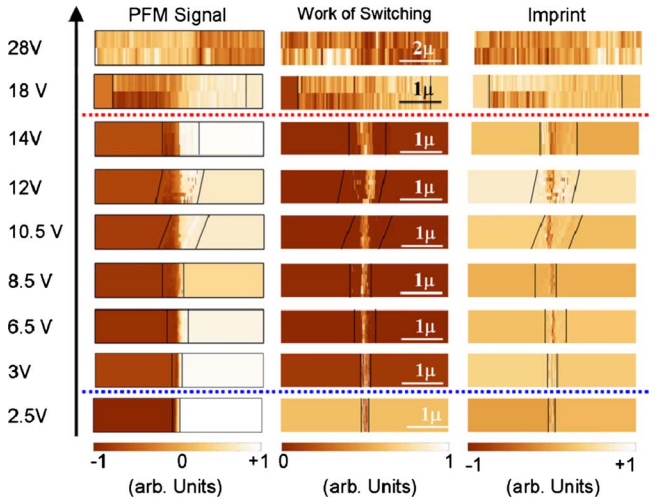


FIG. 2. (Color online) Evolution of the wall dynamics as a function of bias window. Shown are (a) piezoresponse, (b) work of switching, and (c) imprint SS-PFM maps. The images are corrected (aliasing) to compensate for wall creep during measurements.

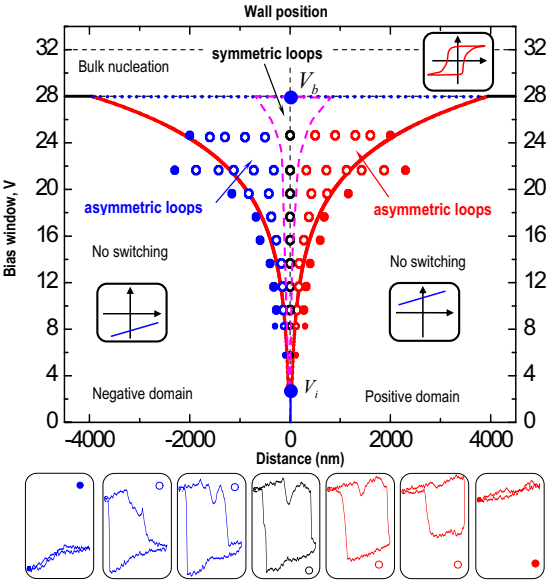


FIG. 3. (Color online) Switching phase diagram showing polarization dynamics as a function of bias window and tip-wall separation. Shown are the regions of no switching, wall-mediated switching with asymmetric loops and symmetric loops (region near $x=0$), and bulk nucleation. Red lines correspond to first-order phase transitions across which the switching loops change discontinuously from open to closed. Blue lines correspond to second-order phase transitions from symmetric to asymmetric switching loops. Blue dotted line marks a continuous transition between wall-mediated and bulk responses. The threshold bias for polarization reversal at the wall is $V_i^*$ and in the bulk is $V_b$. Shown below are experimental PFM hysteresis loops or a bias window of $\pm 14$ V at $x=-220$, $-140$, 0, $+80$, and $+120$ nm.

evolution of the initial response, imprint (i.e., lateral shift of hysteresis loop along the voltage axis), and WoS are shown in Fig. 2. For small bias windows ($<3$ V), the hysteresis loops are closed, WoS is zero, and the initial response map is similar to the PFM image. For bias window $>3$ V, the intermediate contrast region in the initial response image and the white feature in the work of switching image emerge, indicating the onset of domain-wall mobility. As the bias is increased, these features slowly extend into the region far away from the original domain wall. Surprisingly the boundary between the switching and nonswitching regions extends as far as 1 $\mu$m for voltages of 15–25 V. While larger than the 3 V required for nucleation at the domain wall, these are still significantly smaller than the large bias value ($>28$ V) for which the SS-PFM contrast disappears and bulk nucleation is observed everywhere along the surface.

In this intermediate voltage regime, the phase does not show $\sim 180°$ hysteresis at all points. Note that if the amplitude shows a hysteresis behavior but the phase does not show a hysteresis behavior (no 180° switching), the work of switching will still show a high value (because WoS only reflects the mixed piezoresponse). To determine the bulk nucleation field, a point far from domain wall (at least about 5 $\mu$m) was chosen and bias voltage was applied incrementally, starting from low values $\sim 5$ V. It was only at about 28–32 V that switching behavior with 180° shift in the piezoresponse phase hysteresis was observed. Hence, the bulk nucleation was considered to be $\sim 28$ V at a switching frequency of $\sim 1$ Hz (inverse loop acquisition time) and detection frequency of 320 kHz.

Examination of the imprint image reveals an additional difference between the traditional switching through a 2D nucleus on the domain wall and the nucleation mechanism responsible for the nucleation far away from the domain wall at intermediate voltages. The imprint images exhibit a complex structure with imprint almost zero at the wall and forming strong maximum and minimum at the boundaries of the affected region. This behavior is indicative of the strong asymmetry of the hysteresis loop for tip positions to the left and to the right of the domain wall, as can be directly verified by the examination of the loop shape from individual locations (Fig. 3). The dynamic regimes observed as a function of probe-wall separation and bias window are summarized in Fig. 3, delineating the regions of no switching, bulk switching, and wall-mediated switching.

Interestingly, the transition lines in Fig. 3 between no switching and asymmetric switching and between asymmetric and symmetric switching can be classified within the framework of standard theory of phase transitions. Defining a dynamic order parameter $\zeta=\int\{PR^+(V)-PR^-(V)\}dV$, i.e., area under the loop, it is clear that the transition between the no-switching and switching regime is second order (Fig. 4). Similarly, the transition between wall-mediated and bulk switching regimes is first order for order parameter defined as $\xi=\int\{PR^+(V)+PR^-(V)\}dV$, i.e., the average signal.

These experimental studies point at two nontrivial findings regarding the mesoscopic physics of ferroelectric domain wall as explored by SS-PFM. The observations of the minimal tip bias for the domain-wall displacement suggest that the critical bias corresponding to the formation of 2D Miller-Winreich (MW) nucleus is measured directly. We also find that in addition to the standard nucleation mechanisms (formation of the 2D nuclei on the domain wall and bulk nucleation), interaction between the wall and the domain

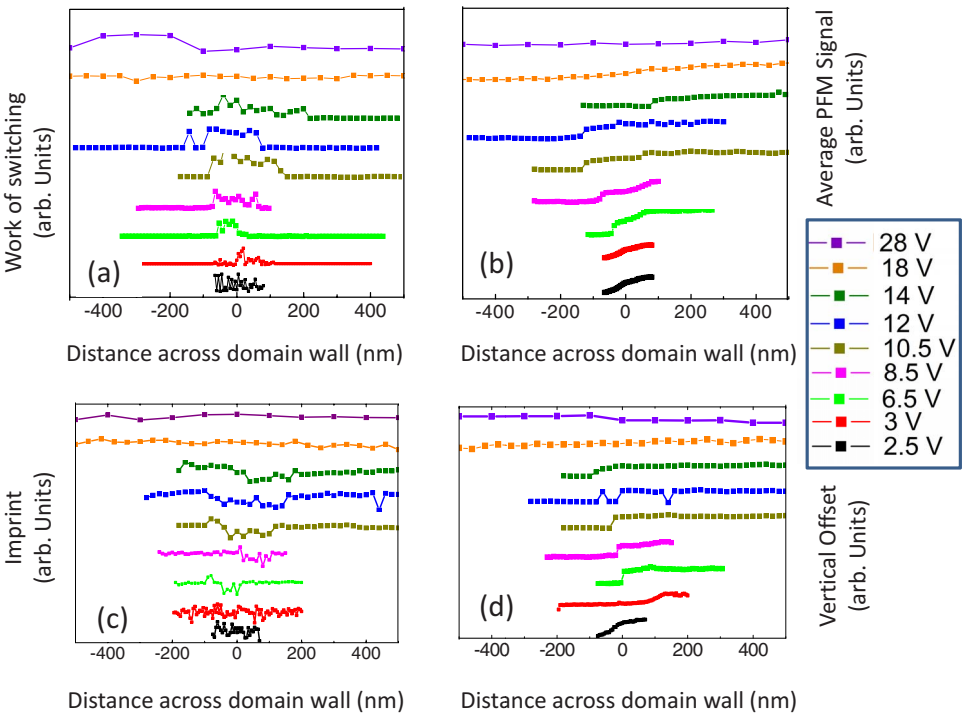


FIG. 4. (Color online) Order-parameters profiles across 180° domain wall in lithium niobate, as the tip sweeps across the domain wall in SS-PFM experiment. (a) Work of switching (total area under the hysteresis loop), (b) average PFM signal (average of all data points on a hysteresis loop), (c) imprint (horizontal offset of the hysteresis loops, along the voltage axis), and (d) vertical offset of the hysteresis loops (along the piezoresponse axis). The legend shown to the right applies to (a), (b), (c), and (d).

nucleus gives rise to a previously unexamined pathway for ferroelectric domain nucleation and switching manifested as an unexpectedly long-range (micron scale) effect of the wall on the domain nucleation bias and loop shape. The nucleation mechanism is analyzed in Sec. III using combination of first-principles, atomistic phase field, and analytical theory. The origins of long-range domain-wall effect on nucleation bias are explored in Sec. IV using combination of analytical theory and phase-field modeling.

## III. 2D NUCLEATION AT DOMAIN WALLS

To get insight into the mechanism of 2D nucleation at the domain wall, we utilize the first-principles density-functional theory (DFT) to obtain estimates of domain-wall energy and the height of the Peierls barrier. This data is combined with the atomistic phase-field model to yield the estimate of nucleation bias and these estimates are further compared with Miller-Weinreich[21] and Burtsev-Chervonobrodov[23] (BC) semiclassical models for 2D nucleation.

### A. Tip parameters estimation

Comparison between the two extremes of bulk nucleation and nucleation at the wall allows us to directly evaluate the activation energy of the 2D nucleus. Bulk nucleation takes place only at the high values of bias (>28 V). Here, the applied electric field destabilizes one of the possible polarization orientations, transforming the potential-energy surface from the ferroelectric double well to a single well, corresponding to the intrinsic switching in the tip-induced field.[26,27] The energy and the electric field required to do this can be estimated from the Landau theory parameters for $LiNbO_3$ (LNO).

The potential distribution induced by the probe, $V_e(x,y)$, was approximated as $V_e(x,y,d) \approx Vd/\sqrt{x^2+y^2+d^2}$, where $V$ is the applied bias and $d$ is the effective probe size.[28] Then we identify the effective size of the tip $d=86$ nm from bulk nucleation bias $V_c=28$ V using $d=V_c\sqrt{27\beta\varepsilon_{11}\varepsilon_0/2\alpha^2}$, where $\alpha=-1.95\times10^9$ m/F and $\beta=3.61\times10^9$ $m^5/(C^2\,F)$ are expansion coefficients of Landau-Ginzburg-Devonshire (LGD) free energy on polarization powers for the second-order uniaxial ferroelectrics, $\varepsilon_0$ is the universal dielectric constant, $\varepsilon_{11}=84$ is the component of the dielectric permittivity transverse to the polarization direction. (see Ref. 22 and Appendix A in the supplementary material[44]).

Note, that in the experiments performed in the ambient conditions (humidity>40%), the bias is applied between the tip apex placed in electric contact with the ferroelectric surface and the bottom electrode. In such a case, a water meniscus appears between the tip apex and the sample surface.[29,30] The meniscus could effectively provide a wider electric contact and prevent the corona discharge appeared for the fields strength $E \approx V/(\gamma d)$ more than the dielectric strength of air (3 MV/m). Allowing for the meniscus appearance and other reasons[28] the effective tip size $d$ determined from the calibration as 86 nm may be noticeably different from the "nominal" tip apex curvature (~10–25 nm).

On the other hand, the water layer below the tip may act as the electrolyte layer with finite mobility that provides the effective screening of the polarization charges outside the sample during the tip-induced polarization reversal. The surface screening charges influence on the polarization switching kinetics everywhere at the surface. A rather complex theoretical description of the effect is far beyond the scope of the present study. Some model cases have been studied previously.[28] Based on these results we expect that the condition of the given potential drop $V_e(x,y,d) \approx Vd/\sqrt{x^2+y^2+d^2}$ may be imposed at the surface $z=0$ to ad-

equately represent the field exerted by the biased tip.

For tip positioned directly at the domain wall, the application of the bias results in wall bending with an associated change in the electromechanical response. Due to the presence of lattice pinning, the formation of a 2D Miller-Weinreich nucleus as the elementary step of wall motion requires a finite probe bias to be applied to the tip, and results in the opening of the hysteresis loop. This behavior is directly observed in Fig. 3, where the potential $V_i$=3 V corresponds to wall unpinning from the lattice, or, equivalently, to formation of a nucleus at the wall.

### B. Domain-wall energetics

We performed the calculations of the domain-wall energy[31] for the domain wall lying at the cation plane and between the anion planes, using both DFT calculations and atomic-level methods with the empirical potential by Jackson *et al.*[32] DFT method is known to be more accurate than empirical method but computationally expensive. DFT calculation yields a Y-wall energy of 160 $mJ/m^2$ when the center of Y wall is between two anion planes (see Fig. 5). For the Y wall at the cation plane, the maximum domain wall energy of 285 $mJ/m^2$. Assuming that this is the maximum in energy, these calculations yield a Peierls barrier to wall motion of 125 $mJ/m^2$. The corresponding analysis using the empirical potential yield an energy of 230 $mJ/m^2$ with the Y-wall center lying between anion planes and 485 $mJ/m^2$ with the center of Y wall at the cation plane. Thus the (presumably less reliable) empirical study yields a Peierls barrier of 255 $mJ/m^2$, which is twice larger value than DFT study. The fit of polarization profile to hyperbolic tangent function derived from LGD theory estimates the domain-wall width of 2.12 Å. The lattice periodicity along the Y wall is 2.58 Å. Thus, the ratio between domain-wall width $\delta$ and the lattice periodicity $d$, $\delta/d$ of 0.82, potentially yielding a high Peierls potential.

### C. Atomic-level phase-field modeling

The quantitative description of the 2D nucleation process at the domain wall is achieved using recently developed diffuse nucleus model. Here, the polarization profile around the nucleus on the domain wall is given by a generalized form of the well-known polarization profile for the 180° domain wall,

$$P_z(x,y,z) \approx 2P_s f^-(x,l_x,\delta_x) f^-(y,l_y,\delta_y) f^-(z,l_z,\delta_z) + P_z^{180}(x-l_x/2,y,z), \quad (1)$$

where $2f^{\pm}(a,b,g)=\tanh[(2a+b)/g] \pm \tanh[(2a-b)/g]$, $l_k$ corresponds to the length of the nucleus to the $k$ direction, and $\delta_k$ corresponds to the diffuseness to the $k$ direction. The $P_z^{180}(x-l_x/2,y,z)$ term corresponds to the polarization profile of the initial flat domain wall.

The free-energy change $\Delta U$ of a nucleus due to the external field $E$ acting on the 180° domain wall is a sum of the local energy, gradient energy, and field-polarization terms and is given by $\Delta U=\Delta U_v+\Delta U_i$, where

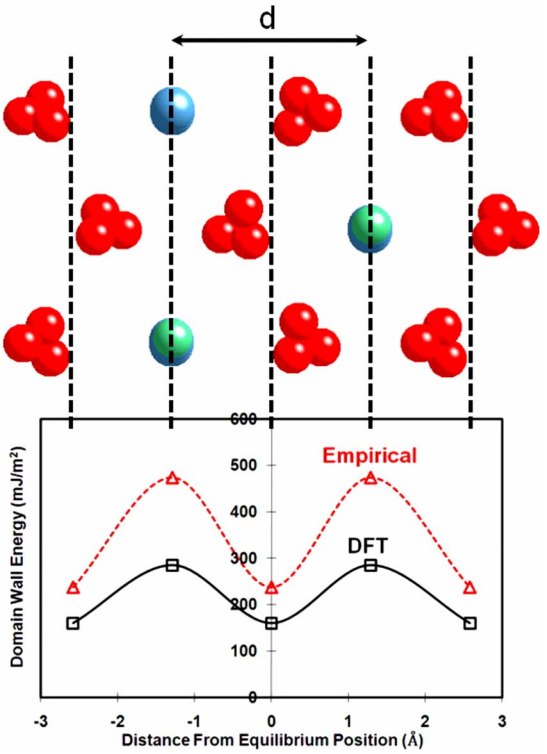


FIG. 5. (Color online) Energies of Y walls at the cation plane and between anion planes. The equilibrium position is determined as the center between two anion planes. The curves are guides to the eye.

$$\Delta U_v = -E\int_{-\infty}^{\infty}\int_{-\infty}^{\infty}\int_{-\infty}^{\infty} dxdydz[P_z(x,y,z) - P_z^{180}(x,y,z)] \quad (2)$$

and

$$\Delta U_i = \int_{-\infty}^{\infty}\int_{-\infty}^{\infty}\int_{-\infty}^{\infty} dxdydz\left\{\left[g_x\left(\frac{\partial P_z}{\partial x}\right)^2 + g_y\left(\frac{\partial P_z}{\partial y}\right)^2 + g_z\left(\frac{\partial P_z}{\partial z}\right)^2 + U_{loc}(P_z)\right] - \left[g_x\left(\frac{\partial P_z^{180}}{\partial x}\right)^2 + U_{loc}(P_z^{180})\right]\right\}. \quad (3)$$

The subscripts $v$ and $i$ refer to *volume* and *interface*, respectively. The local contribution is $U_{loc}(p)=A_{loc}[1-(p/p_s)^2]^2$, where $A_{loc}$ is the ferroelectric well depth at 0 K and $g_x$ and $g_z$ parametrize the energy cost of longitudinal and transverse polarization changes. The contribution of the depolarization energy is ignored as it is negligible for a small nucleus.[21] Therefore, parameters $A_{loc}(T)$, $g_x$, $g_z$, and $P_s(T)$ are necessary to evaluate the energy of the critical nucleus.

The temperature dependence of $A_{loc}(T)$ is obtained from the DFT $A_{loc}$ at 0 K and the ratio of the experimental $P_s$ at finite temperature and at 0 K. For $LiNbO_3$, the 0 K DFT polarization is ~0.8 $C/m^2$ (Ref. 33). The $g_x$ parameter is proportional to the square root of $(\sigma_{100}/P_s)^2/A_{loc}$, where $\sigma_w$ is the 180° domain-wall energy and $P_s$ is the 0 K polarization [see Eq. (16) in supplementary material[44] for Ref. 24]. To

evaluate $g_x$, we used the DFT value of the $LiNbO_3$ 180° domain-wall energy $\sigma_w=0.160$ J/m$^2$ and $A_{loc}=0.25$ eV (Ref. 34). This results in $g_x$ value of $9.9\times10^{-12}$ m$^3$/F. To estimate the $g_z$ gradient parameter, we use the $LiNbO_3$ $g_x$ value and the ratio between $g_z$ and $g_x$ ($g_z/g_x=1.7$) previously found for $PbTiO_3$. The $g_z$ parameter is then equal to $1.68\times10^{-11}$ m$^3$/F.

Using the electric field strength, estimated as $5\times10^7$ V/m from the expression $E\approx V/(\gamma d)$ at $d=86$ nm, dielectric anisotropy factor $\gamma=0.24$ and experimentally observed voltage of 3 V at the domain wall and solving numerically for the polarization profile with minimum energy at different $l_k$ and $\delta_k$, we obtain that $l_y\sim12$ Å, $l_z\sim20$ Å, $\delta_y\sim4$ Å, $\delta_z\sim6$ Å and a critical nucleus energy of 0.17 eV or about $7k_BT$, sufficient for almost instantaneous nucleation. Although there are several sources of uncertainty in the calculation of the critical nucleus energy, such as the variation in the values of $A_{loc}$ and room temperature $P_s$ (e.g., see Ref. 35), these will not change the value of the critical nucleus energy by a large enough amount to make the nucleation time longer or comparable to the experimental, approximately millisecond, time scale. This suggests that the activation barrier for 2D nucleation at the wall is controlled by the thermally activated process.

### D. Semiclassical models for 2D nucleation

The atomistic model in Sec. III C estimates the activation barrier for 2D domain nucleation as 0.17 eV, if the depolarization field effects are ignored. In this section, we analyze the effects of depolarization contributions on the 2D nucleation using extensions of MW and BC models. We note that MW considered the lattice discreteness in very oversimplified model and do not take the possibility of the wall bending into account. Furthermore, the wall is regarded infinitely thin. In contrast to MW smooth BC (Ref. 23) approach considered much more realistic model with continuous lattice potential and diffuse domain walls, at that the nucleus shape and domain-wall width are calculated self-consistently.

For the MW model, the activation energy for 2D rigid nucleus formation in the electric field of a biased PFM tip averaged over the nucleus volume is given by

$$F_a^{\mathrm{MW}}(\sigma_w,V,x_0)=\frac{8}{3\sqrt{3}}\sqrt{\ln\left(\frac{\langle\sigma_w\rangle\theta}{2cP_sd^2V}\right)}\frac{(c\langle\sigma_w\rangle)^3}{\pi\varepsilon_0\varepsilon_{11}}\frac{\theta}{d^2V}, \quad (4)$$

where $\sigma_w$ is the domain-wall energy, parameter $\theta=\gamma(\sqrt{d^2+x_0^2})^3$ originated from the averaging of the tip electric field,

$$E_3=\frac{V(d+z/\gamma)d}{\gamma[(d+z/\gamma)^2+\rho^2]^{3/2}} \quad (5)$$

over the nucleus volume ($\rho=\sqrt{x^2+y^2}$), $c$ is the lattice constant, $\gamma=\sqrt{\varepsilon_{33}/\varepsilon_{11}}$ is the dielectric anisotropy factor, $x_0$ is the distance between the tip apex and the wall (see Appendix B in the supplementary material[44] for details). The $LiNbO_3$ materials parameters are $c=0.5$ nm, $P_s=0.75$ C/m$^2$, $\varepsilon_{11}=84$, and $\varepsilon_{33}=30$. The domain-wall energy $\langle\sigma_w\rangle=\sigma_{\min}+\delta\sigma/2$ was calculated using density-functional theory as $\sigma_w(x)\approx\sigma_{\min}+\delta\sigma\sin^2[\pi(x-x_0)/c]$, where $\sigma_{\min}=0.160$ J/m$^2$ and periodic lattice potential $\delta\sigma=0.125$ J/m$^2$.[31] The activation barrier calculated using Eq. (1) for applied voltage of 3 V and $d=86$ nm is significantly larger than $50k_BT$. The expected observation time $t=t_0\exp(-F_a/k_BT)\sim10^8$ s at phonon times $t_0=10^{-12}$ s, which is too high to account for reasonable experimental time. We estimate that according to MW model an applied voltage of 16–21 V would be required to unpin the domain wall from the lattice at $x_0=0$ (see Table I in Appendix B in the supplementary material[44]).

Using BC approach we obtained the barrier directly at the wall ($x_0=0$),

$$F_a^{\mathrm{BC}}(\sigma_w,V,x_0=0)=\sqrt{\ln\left(\frac{\gamma d\sqrt{\sigma_{\min}\delta\sigma}}{2cP_sV}\right)}\frac{(c\sqrt{\sigma_{\min}\delta\sigma})^3}{4\pi\varepsilon_0\varepsilon_{11}}\frac{\gamma d}{V}. \quad (6)$$

Let us underline the following distinctions between MW and expression (6): (1) replacement of $\langle\sigma_w\rangle=\sigma_{\min}+\delta\sigma/2$ with $\sqrt{\sigma_{\min}\delta\sigma}$, where $\sigma_{\min}$ is the minimal value of potential and $\delta\sigma$ is the modulation depth. (2) Due to the domain-wall diffuseness, a subcritical nucleus has a very smooth shape and factor $16\sqrt{3}/9\approx3.2$ disappears.

Equation (2) yields nucleation potential of 3.6 V for observation time ~10 ms (corresponding to barrier $25k_BT$) and 10.5 V for instant nucleation (corresponding to barrier of $1k_BT$). Note that these estimates are very close to that of the atomistic model, with primary uncertainly related to numerical values of LNO parameters and the contribution of depolarization field of the nucleus, and are fully consistent with experimental observations.

## IV. LONG-RANGE MESOSCOPIC DYNAMICS AT THE FERROELECTRIC WALL

The examination of the diagram in Fig. 3 illustrates the presence of the long-range interactions in the system exhibited as long-range effects of preexisting domain wall on nucleation bias and hysteresis loop shape. The nucleation bias is reduced by ~10% compared to bulk values at distances as large as ~2–3 $\mu$m, which is ~30 larger then tip radius estimated from either spatial resolution or bulk nucleation bias. To get insight into origins of this behavior, we perform the extensive phase-field modeling of switching process, and develop an analytical long-range interaction model.

### A. Phase field modeling of long-range interaction effects

The mesoscale mechanism of polarization switching in $LiNbO_3$ under PFM tip is further modeled using the phase-field approach[36] in which the ferroelectric domain is described by the spatial distribution of the polarization vector $\vec{P}(\mathbf{x})$. The temporal evolution of polarization $\vec{P}(\mathbf{x})$ is obtained by solving the time-dependent Ginzburg-Landau equation,

$$\frac{\partial P_i(\mathbf{x},t)}{\partial t}=-L\frac{\delta F}{\delta P_i(\mathbf{x},t)} \quad (i=1,2,3), \quad (7)$$

where $L$ is the kinetic coefficient associated with domain-wall mobility and $F$ is the free-energy functional. The free

energy functional includes bulk, domain wall, elastic, and electrostatic energies as $F=\int_V(f_{bulk}+f_{grad}+f_{elas}+f_{elec})dV$.

For LNO, the bulk free energy $f_{bulk}$ is described by the Landau polynomial expansion as follows:

$$f_{bulk}=\alpha_1 P_3^2+\alpha_{11}P_3^4+\alpha_2(P_1^2+P_2^2), \tag{8}$$

where $\alpha_1=-1.0\times10^9$ $C^{-2}$ $m^2$ N, $\alpha_{11}=0.9025\times10^9$ $C^{-4}$ $m^6$ N, and $\alpha_2=0.9725\times10^9$ $C^{-2}$ $m^2$ N at room temperature. The gradient energy density $f_{grad}$ is nonzero at the domain walls and is described by

$$f_{grad}=\frac{1}{2}G_{11}(P_{1,1}^2+P_{1,2}^2+P_{2,1}^2+P_{2,2}^2+P_{3,1}^2+P_{3,2}^2)$$
$$+\frac{1}{2}G_{22}(P_{1,3}^2+P_{2,3}^2+P_{3,3}^2), \tag{9}$$

where $P_{i,j}=\frac{\partial P_i}{\partial x_j}$, $G_{11}=G_{22}=0.4G_0$, $G_0=\alpha_0(\Delta x)^2$, $\alpha_0=-\alpha_1$, and $\Delta x$ is the grid size of the simulation box. The elastic energy $f_{elas}$ arises from the electrostrictive strains,

$$f_{elast}=\frac{1}{2}C_{ijkl}(e_{ij}-e_{ij}^o)(e_{kl}-e_{kl}^o), \tag{10}$$

where $C_{ijkl}$ is the elastic stiffness tensor, $e_{ij}$ is the total strain, and $e_{ij}^o=Q_{ijkl}P_kP_l$ with $Q_{ijkl}$ representing the electrostrictive coefficients. The nonzero elastic stiffness and electrostrictive coefficients in the Voigt's notation are $C_{11}=1.99\times10^{11}$ N $m^{-2}$, $C_{12}=0.55\times10^{11}$ N $m^{-2}$, $C_{44}=0.6\times10^{11}$ N $m^{-2}$, $Q_{11}=0.016$ $C^{-2}$ $m^4$, $Q_{12}=-0.003$ $C^{-2}$ $m^4$, and $Q_{44}=0.019$ $C^{-2}$ $m^4$. The elastic solution, $e_{ij}$, is obtained by solving the elasticity equation, $C_{ijkl}\nabla_j[(e_{kl}-e_{kl}^o)]=0$ using a combination[37] of Khachaturyan theory of elasticity[38,39] and Stroh's algorithm.[40]

Finally, the electrostatic energy density of an inhomogeneous polarization distribution under an applied electric field, $E_i^{ex}$, is $f_{elec}=-\frac{1}{2}E_iP_i-E_i^{ex}P_i$, where $E_i$ is the electrical field generated by the inhomogeneous polarization that does not include the external field contribution. The first term is the electrostatic energy of an inhomogeneous polarization distribution and the second term is the coupling energy between the external field and polarization distribution. In terms of total electric field, $E_i$, which includes both the electric field due to polarization inhomogeneity and the external field, the corresponding energy component is $f_{elec}=-1/2\varepsilon_{ij}^b\varepsilon_oE_iE_j-E_iP_i$, $\varepsilon_{ij}^b$ is the relative background permittivity (~7–10) (Ref. 41) and $\varepsilon_o=8.85\times10^{-12}$ F $m^{-1}$ is the dielectric permittivity of vacuum. The electric field is obtained by solving the Poisson equation for the electric potential, $-\varepsilon_{ij}^b\varepsilon_o\nabla_i\nabla_j\phi=-\nabla_iP_i$, using a similar method to the elasticity solution.[42]

Equation (7) is solved using the Fourier spectral method on a $128\Delta x\times128\Delta x\times64\Delta x$ domain with periodic boundary conditions along $x_1$ and $x_2$ axes. The film thickness is $h_f=56\Delta x$. The critical bulk nucleation potential is obtained by gradually increasing the potential $\phi_0$ at the tip in steps of 0.05 V until a new domain is observed.

The switching diagram of the tip bias voltage required for switching (i.e., for observing open PFM loops) as a function of the distance from the wall, determined from phase-field simulations, is shown in Fig. 6. The circles in the figure are estimated using phase-field simulations. The open circles represent the open loops and the closed loops are indicated by filled circles. The distances and the bias window voltage values are calibrated using experimental data. Also shown in the dotted line is an approximate fit to the experimental data points from Fig. 3. A series of typical polarizations hysteresis loops at different tip positions for a fixed bias voltage of 16 V are shown in Fig. 6(b). Note the excellent agreement between the experimental and theoretical switching diagrams. Here, we focus our comparison on two specific aspects of this diagram, namely, (1) the switching threshold bias at the domain wall versus away from the wall and (2) the long-range influence of the wall up to several micrometers.

Interestingly, the phase-field modeling suggests the presence of a threshold field for domain-wall motion, despite the fact that the lattice-level pinning is not included explicitly. The threshold bias using phase-field modeling is finite and the magnitude of this bias depends on the number of time steps for which the system was relaxed under a bias field. In general for a shorter period of relaxation, kinetic effects are still dominant and the bias threshold at the wall is higher. For example, for ~100 time steps, the bias threshold is ~3 V, close to experimental results. For long relaxation times, the system approaches a steady-state threshold of ~0.3 V. The same value of steady-state threshold bias was also observed for a simulation of the wall system under a uniform electric field instead of a biased tip and likely represents the effects of the spatial discretization grid in the phase-field model. Overall, this suggests that experimentally observed 3 V threshold corresponds to the formation of 2D nucleus controlled by the lattice periodicity effects.

The long range influence of the wall can be understood by tracking the domain-wall evolution with time around a hysteresis loop, as shown in Fig. 7. For tip biases below the bulk nucleation bias of 28 V, the switching mechanism is predominantly governed by the attraction and repulsion of the wall due to the nearby tip. An opening in the polarization loop is observed when the wall bends and crosses past the region under the tip, and retraces back under a reverse bias. The asymmetry in the polarization loop arises from this fact in which the loop opening occurs only for the bias that bends the wall toward the tip.

### B. Analytical studies

To decipher the origins of long-range wall-tip interactions, we analyze the mesoscopic mechanism of polarization switching in the presence of an initially flat 180° domain wall and in the absence of the lattice pinning. The dynamics of the polarization field, $P_3$, is described by the Landau-Ginzburg-Devonshire-Khalatnikov relaxation equation,

$$-\tau\frac{d}{dt}P_3=\alpha P_3+\beta P_3^3-\eta\left(\frac{\partial^2P_3}{\partial z^2}+\frac{\partial^2P_3}{\partial x^2}+\frac{\partial^2P_3}{\partial y^2}\right)-E_3, \tag{11}$$

where $\tau$ is the Khalatnikov coefficient, $\alpha<0$ in ferroelectric phase, the gradient term $\eta>0$, expansion coefficient $\beta>0$ for the second-order phase transitions considered hereinafter.

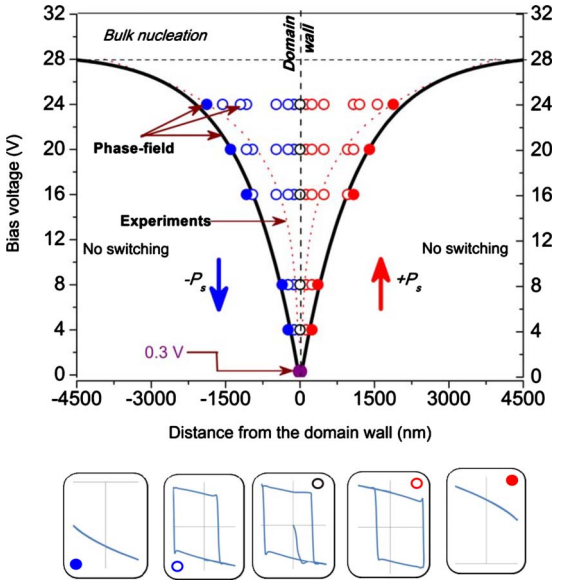


FIG. 6. (Color online) (a) Phase-field prediction of switching phase diagram. The open and closed circles, calculated using phase-field simulations, represent the open and closed loops, respectively. The broken red line is an approximate fit to the experimental data from Fig. 3 and the solid black line is an approximate fit to the phase-field predictions. The phase-field limit for nucleation bias at the wall is ~0.3 V for 1000 steps relaxation (as compared to 0 in ideal model). The $x$ and $y$ axes in phase field were calibrated using experimental values. (b) Five representative polarization hysteresis loops at steady state at different tip positions (−1080 nm, −120 nm, 0 nm, +120 nm, +1080 nm) from the wall at a fixed tip bias voltage of 16 V.

The polarization boundary conditions are $P_3 - \lambda \partial P_3/\partial z = 0$ at the surface.

Electric field $E_3(x,y,z) = -\partial\varphi/\partial z$, where the electrostatic potential distribution, $\varphi(\mathbf{r})$, in ferroelectric is coupled with polarization as

$$\varepsilon_0 \varepsilon_{33}^b \frac{\partial^2 \varphi}{\partial z^2} + \varepsilon_0 \varepsilon_{11} \left( \frac{\partial^2 \varphi}{\partial x^2} + \frac{\partial^2 \varphi}{\partial y^2} \right) = \frac{\partial P_3}{\partial z}, \tag{12}$$

where $\varepsilon_{33}^b \leq 10$ is the dielectric permittivity of background state[41] and $\varepsilon_0$ is the universal dielectric constant. $\varepsilon_{11}$ and $\varepsilon_{33} \gg \varepsilon_{33}^b$ are dielectric permittivity values perpendicular and along polar axis $z$. The potential distribution induced by the probe yields boundary conditions $\varphi(\rho, z=0) = V(t)d/\sqrt{\rho^2+d^2}$, where $V$ is the applied bias and $d$ is the effective probe size, hereinafter $\rho = \sqrt{x^2+y^2}$.

Allowing for the superposition principle, the electric field that satisfy Eq. (5) is the sum $E_3(x,y,z) = E_3^e(x,y,z) + E_3^d(x,y,z)$, where $E_3^e(x,y,z)$ is the probe field inside the sample and $E_3^d(x,y,z)$ is the depolarization field created by the curved domain wall.[43] Expressions for the fields are listed in Appendix A of the supplementary material.[44] Note that ferroelectric cubic nonlinearity ($\sim \beta P_3^3$) and the order-parameter spatial dispersion (polarization gradient) determine only the short-range correlation effects between the domain nucleus and the wall, which dominate at distances $|x_0| \leq d$. However the Coulombic electric field is mainly responsible for the long-range interaction between the slightly curved domain walls and the probe-induced domain nucleus located even far enough (i.e., at $|x_0| \gg d$) from the walls. Actually, the power decay of Coulombic field possibly results in correlated switching at distances more than 100 nm.

Using direct variational method for polarization redistribution $P_3(x,y,z,t) \approx P_0(x) + P_V(t) f(x,y,z)$, where $P_0(x) = P_s \tanh[(x-x_0)/2L_\perp]$ is the initial flat domain-wall profile positioned at $x = x_0$ (the correlation length is $L_\perp = \sqrt{-\eta/2\alpha}$ and the spontaneous polarization is $P_s^2 = -\alpha/\beta$). The coordinate-dependent part $f(\rho,z) \approx \frac{\sqrt{\varepsilon_{11}\varepsilon_0/(-2\alpha)}d^2}{(L_\perp d + d^2 + \rho^2)\sqrt{d^2+\rho^2}}$ satisfy the linearized Eq. (4). The parameter $P_V$ serves as effective variational parameter describing domain geometry and allows reducing complex problem of domain dynamics in the nonuniform field to an algebraic equation obtained after the

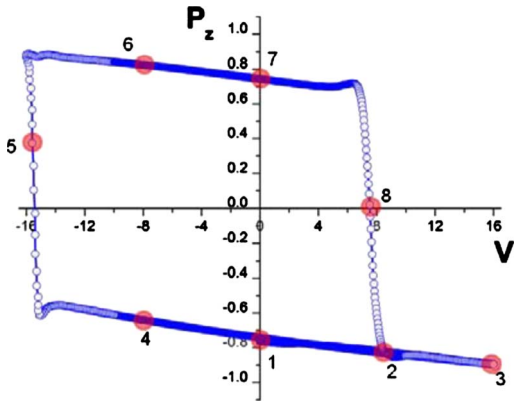


(a)

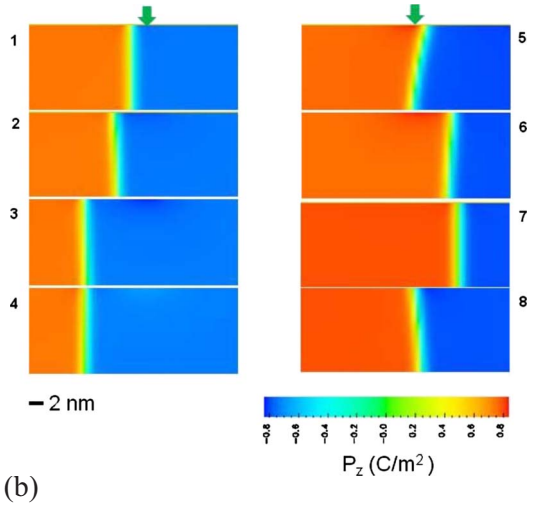


(b)

FIG. 7. (Color online) Phase-field modeling results: (a) an asymmetric polarization hysteresis loop at a fixed tip bias of 16 V when the tip is positioned on the negative domain ($-P_s$) away from the wall. (b) Eight representative sections showing the evolution of the domain wall with time around the hysteresis loop. The sections correspond to the points marked with red circles and labeled 1–8 in the hysteresis loop on the left. The attraction and repulsion of the wall due to the nearby tip results in asymmetric switching.

substitution of $P_3(x,y,z,t)$ into the LGD free-energy functional, integration, and minimization on $P_V$.[22]

Thus we derived that in the presence of lattice pinning of viscous friction type, the amplitude $P_V$ should be found from the equation of Landau-Khalatnikov type,

$$\tau\frac{d}{dt}P_V + w_1 P_V + w_2(x_0)P_V^2 + w_3 P_V^3 = V(t), \qquad (13)$$

where constants $w_i$ describe tip geometry and materials properties as[22]

$$w_1 \approx 1, \quad w_2(x_0) \approx \frac{-3\beta P_s x_0}{\sqrt{(L_\perp + d)^2 + x_0^2}} \frac{\sqrt{-2\alpha\varepsilon_{11}\varepsilon_0}}{4\alpha^2(L_\perp + d)},$$

$$w_3 \approx \frac{\beta\varepsilon_{11}\varepsilon_0}{4\alpha^2(L_\perp + d)^2}. \qquad (14)$$

Equations (4)–(7) provide comprehensive description of polarization dynamics in the vicinity of the wall and in the bulk.

Introducing the new parameter $P = P_V \frac{\sqrt{-2\alpha\varepsilon_{11}\varepsilon_0}}{-2\alpha(L_\perp+d)} - P_s$, one can rewrite the static Eq. (6) as

$$\alpha P[6n(x_0) - 5] + \beta P^3 + 3\beta P^2 P_s[1 - n(x_0)]$$
$$= \frac{\sqrt{-2\alpha\varepsilon_{11}\varepsilon_0}V}{L_\perp + d} - 3\beta P_s^3[1 - n(x_0)]. \qquad (15)$$

Let us underline that the terms determined by the function $n(x_0) = x_0/\sqrt{(L_\perp+d)^2+x_0^2}$ originated from nonlinear (cubic) interactions of the probe field and the stray depolarization field with initially flat domain wall. As the result wall curvature or domain nucleation appears.

Far from wall ($x_0 \gg d$) the Eq. (8) reduces to the usual symmetric ferroelectric hysteresis $\alpha P + \beta P^3 = V\sqrt{-2\alpha\varepsilon_{11}\varepsilon_0}/(L_\perp + d)$. Near the wall ($x_0 \ll d$) Eq. (S.7) gives equation $-5\alpha P + \beta P^3 + 3\beta P^2 P_s = \frac{\sqrt{-2\alpha\varepsilon_{11}\varepsilon_0}V}{L_\perp+d} - 3\beta P_s^3$ that possesses no hysteresis because of negative $\alpha$.

Static thermodynamic coercive biases $V_c^{\pm}(x_0)$ are determined from $dV/dP_V = 0$. The expected behavior of the hysteresis loops as a function of tip surface separation is illustrated in Fig. 8. Directly at the wall, the loop is closed and the local response originates from the bias-induced bending of the domain wall. The bistability is possible for $x_0^2 \geq 2(L_\perp + d)^2$. The loop width, determined as the difference of coercive biases $\Delta V_c = (V_c^+ - V_c^-)/2$, monotonically increases with the distance $x$. Far from wall ($x_0 \gg d$) corresponding coercive biases are symmetric, $V_c^\infty = \pm 2\alpha P_s(L_\perp + d)/\sqrt{-54\alpha\varepsilon_{11}\varepsilon_0}$. The inclusion of viscous friction leads to the loop broadening and smearing far from the wall while near the wall the minor loop opening is observed (compare solid and dotted curves). Note that the qualitative evolution of hysteresis loops in Fig. 8 is highly reminiscent of the experimental data in Fig. 3.

## V. SUMMARY

To summarize, ferroelectric domain walls, long believed to be the simplest example of *static* topological defect in ferroic materials, are found to exhibit an unexpectedly rich panoply of nanoscale switching behaviors due to interplay between wall bowing and bulklike nucleation. The effective nucleation bias is found to increase by an order of magnitude from a 2D nucleus at the wall to 3D nucleus in the bulk. The effect of the wall is extremely long range with significantly lower nucleation bias even for tip-wall separation in the micrometer range. This is due to the compensation of depolarization field of nascent domain by wall bowing. Notably, the nucleation bias at the wall (3 V) allows a direct measurement of the nucleation energy for the 2D nucleus, which is found to be well below that predicted by rigid ferroelectric (Miller Weinreich)[21] models (~16–21 V), but is in a reasonable agreement with the smooth lattice potential models (Burtsev-Chervonobrodov)[23] (~3–7 V) and in excellent agreement with recently developed diffuse nucleus model.[24]

Our studies open a pathway to detailed atomistic understanding of domain-wall dynamic in ferroic materials, including wall-defect interactions (pinning), structure, and behavior of the walls with coupled order parameters, and dynamic effects such as nucleation in front of the moving wall. In these, the biased probe represents local charged defect of controlled strength. These studies become increasingly important given the rapidly growing role of ferroelec-

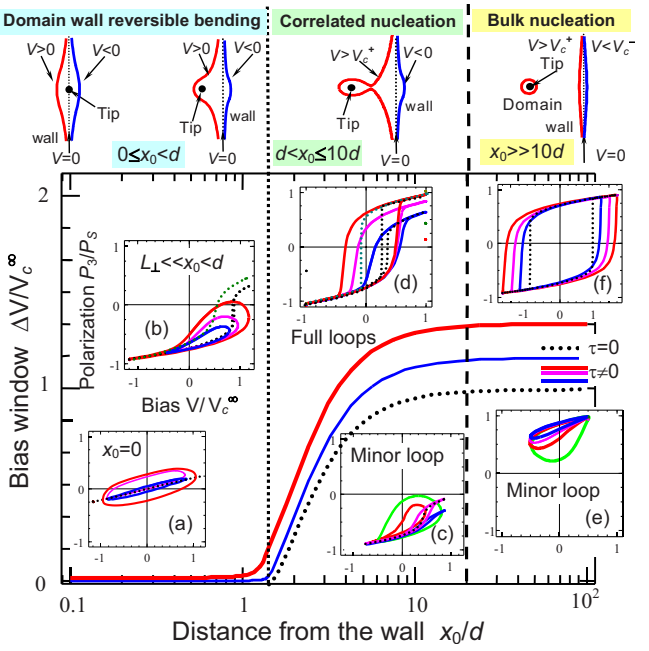


FIG. 8. (Color online) Map of the switching regimes (upper row) and corresponding ferroelectric polarization hysteresis loop shape [insets (a)–(e)] depending on the wall-tip separation, $x_0$, calculated from the analytical theory. Dotted curve [and loops (a)–(e)] is plotted for the static case $\tau = 0$, solid curves [and loops (a)–(e)] correspond to the kinetic case with $\tau \neq 0$. The reversible wall bending occurs at $0 < x_0 < d$, correlated nucleation occurs at $d < x_0 < 10d$, and symmetric bulk nucleation starts at $x_0 \gg 10d$. Curves correspond to the different relaxation coefficients $\tau = 0$, $10^{-8}$, $10^{-7}$, $10^{-6}$ SI units. Material parameters for $LiNbO_3$ are $L_\perp = \sqrt{-\eta/2\alpha} \sim 0.5$ nm, extrapolation length $\lambda \gg L_\perp$, $\eta = 10^{-9}$ m$^3$/F, $\varepsilon_{11} = 84$, $\varepsilon_{33} = 30$, $\alpha = -2 \times 10^9$ SI units, $\beta = 3.61 \times 10^9$ m$^5$/(C$^2$ F), $P_s = 0.75$ C/m$^2$, and frequency $\omega = 2\pi \times 10^4$ rad s$^{-1}$.

trics and multiferroics in information and energy storage technologies.

Finally, we expect that the fundamental mechanisms explored in this work—namely, the lowering of the potential barrier to the nucleation of a new phase induced by the presence of (mobile) interface due to screening of long-range electrostatic and elastic fields—will be applicable to a broad range of electrochemical and solid-solid phase transformations.

## ACKNOWLEDGMENTS

Research supported in part (S.V.K., S.J., and K.S.) by Scientific User Facilities Division, U.S. DOE. V.R.A. and V.G. acknowledge the CNMS user program. V.G. acknowledges NSF under Grants No. DMR-0820404, No. DMR-0908718, and No. DMR-0602986. D.L. and S.R.P. acknowledge NSF under Grant No. DMR-0602986. A.N.M. and S.V.S. acknowledge joint Russian-Ukrainian grant NASU under Grant No. N 17-Ukr_a (RFBR under Grant No. N 08-02-90434). V.G. thanks K. Kitamura and K. Terabe for providing the thin LNO crystal. Research sponsored by Ministry of Science and Education of Ukrainian (Grant No. UU30/004) and National Science Foundation (Materials World Network, Grant No. DMR-0908718). The authors acknowledge multiple discussions with J. F. Scott, P. Paruch, A. Levanyuk, A. Gruverman, and A. K. Tagantsev and thank them for invaluable advices. V.R.A. was previously known by the name Aravind Vasudevarao. A. M. R. acknowledges support from DOE, under Grant No. DE-FG02-07ER15920. I. G. acknowledges support from ONR under Grant No. N00014-09-1-0157.

*vgopalan@psu.edu
†sergei2@ornl.gov

[1] A. K. Tagantsev, L. E. Cross, and J. Fousek, *Ferroelectric Domains in Ferroelectric Crystals and Thin Films* (Springer, New York, 2010).
[2] *Lithium Batteries: Science and Technology*, edited by G. A. Nazri and G. Pistoia (Springer-Verlag, New York, 2009).
[3] *Lithium Ion Rechargeable Batteries*, edited by K. Ozawa (Wiley, Weinheim, 2009).
[4] R. A. Huggins, *Advanced Batteries: Materials Science Aspects* (Springer-Verlag, New York, 2008).
[5] V. Wadhawan, *Introduction to Ferroic Materials* (CRC Press, Cleveland/Boca Raton, 2000).
[6] J. Scott, *Ferroelectric Memories* (Springer-Verlag, Berlin, 2000).
[7] *Nanoelectronics and Information Technology*, edited by R. Waser (Wiley-VCH, Berlin, 2005).
[8] W. J. Merz, J. Appl. Phys. **27**, 938 (1956).
[9] A. S. Sidorkin, *Domain Structure in Ferroelectrics and Related Materials* (Cambridge International Science, Great Abington, Cambridge, 2006).
[10] T. Nattermann, Y. Shapir, and I. Vilfan, Phys. Rev. B **42**, 8577 (1990).
[11] P. Paruch, T. Giamarchi, and J. M. Triscone, Phys. Rev. Lett. **94**, 197601 (2005).
[12] V. Repain, M. Bauer, J. P. Jamet, J. Ferre, A. Mougin, C. Chappert, and H. Bernas, Europhys. Lett. **68**, 460 (2004).
[13] C. L. Jia, S. B. Mi, K. Urban, I. Vrejoiu, M. Alexe, and D. Hesse, Nature Mater. **7**, 57 (2008).
[14] M. W. Chu, I. Szafraniak, D. Hesse, M. Alexe, and U. Gosele, Phys. Rev. B **72**, 174112 (2005).
[15] L. M. Eng, H. J. Guntherodt, G. A. Schneider, U. Kopke, and J. M. Saldana, Appl. Phys. Lett. **74**, 233 (1999).
[16] C. S. Ganpule, A. L. Roytburd, V. Nagarajan, B. K. Hill, S. B. Ogale, E. D. Williams, R. Ramesh, and J. F. Scott, Phys. Rev. B **65**, 014101 (2001).
[17] P. Paruch, T. Giamarchi, T. Tybell, and J. M. Triscone, J. Appl. Phys. **100**, 051608 (2006).
[18] V. Gopalan, Q. X. Jia, and T. E. Mitchell, Appl. Phys. Lett. **75**, 2482 (1999).
[19] V. Ya. Shur, E. L. Rumyantsev, A. G. Shur, A. I. Lobov, D. K. Kuznetsov, E. I. Shishkin, E. V. Nikolaeva, M. A. Dolbilov, P. S. Zelenovskiy, K. Gallo, and M. P. De Micheli, Ferroelectrics **354**, 145 (2007).
[20] V. Ya. Shur, A. Gruverman, N. Yu. Ponomarev, E. L. Rumyantsev, and N. A. Tonkachyova, Integr. Ferroelectr. **2**, 51 (1992).
[21] R. Miller and G. Weinreich, Phys. Rev. **117**, 1460 (1960).
[22] A. N. Morozovska, S. V. Kalinin, E. A. Eliseev, V. Gopalan, and S. V. Svechnikov, Phys. Rev. B **78**, 125407 (2008).
[23] E. V. Burtsev and S. P. Chervonobrodov, Ferroelectrics **45**, 97 (1982).
[24] Y. H. Shin, I. Grinberg, I. W. Chen, and A. M. Rappe, Nature (London) **449**, 881 (2007).
[25] S. Jesse, H. N. Lee, and S. V. Kalinin, Rev. Sci. Instrum. **77**, 073702 (2006).
[26] S. V. Kalinin, B. J. Rodriguez, S. Jesse, Y. H. Chu, T. Zhao, R. Ramesh, E. A. Eliseev, and A. N. Morozovska, Proc. Natl. Acad. Sci. U.S.A. **104**, 20204 (2007).
[27] P. Maksymovych, S. Jesse, M. Huijben, R. Ramesh, A. Morozovska, S. Choudhury, L. Q. Chen, A. P. Baddorf, and S. V. Kalinin, Phys. Rev. Lett. **102**, 017601 (2009).
[28] A. N. Morozovska, S. V. Svechnikov, E. A. Eliseev, S. Jesse, B. J. Rodriguez, and S. V. Kalinin, J. Appl. Phys. **102**, 114108 (2007).
[29] B. L. Weeks, M. W. Vaughn, and J. J. DeYoreo, Langmuir **21**, 8096 (2005).
[30] C. Teschke and E. F. de Souza, Appl. Phys. Lett. **82**, 1126 (2003).
[31] D. Lee, H. X. Xu, V. Dierolf, V. Gopalan, and S. R. Phillpot, Phys. Rev. B **82**, 014104 (2010).
[32] A. Jackson and M. E. G. Valerio, J. Phys.: Condens. Matter **17**, 837 (2005).
[33] M. Veithen and Ph. Ghosez, Phys. Rev. B **65**, 214302 (2002).
[34] I. Inbar and R. E. Cohen, Phys. Rev. B **53**, 1193 (1996).
[35] W. G. Schmidt, M. Albrecht, S. Wippermann, S. Blankenburg, E. Rauls, F. Fuchs, C. Rödl, J. Furthmüller, and A. Hermann, Phys. Rev. B **77**, 035106 (2008).
[36] L. Q. Chen, J. Am. Ceram. Soc. **91**, 1835 (2008).
[37] Y. L. Li, S. Y. Hu, Z. K. Liu, and L. Q. Chen, Acta Mater. **50**,

395 (2002).
[38] A. G. Khachaturyan, *Theory of Structural Transformations in Solids* (Wiley, New York, 1983).
[39] A. G. Khachaturyan and G. A. Shatalov, Sov. Phys. JETP **29**, 557 (1969).
[40] A. N. Stroh, J. Math. Phys. **41**, 77 (1962).
[41] A. K. Tagantsev and G. Gerra, J. Appl. Phys. **100**, 051607 (2006).
[42] Y. L. Li, S. Y. Hu, Z. K. Liu, and L. Q. Chen, Appl. Phys. Lett. **81**, 427 (2002).
[43] A. N. Morozovska, E. A. Eliseev, Y. Li, S. V. Svechnikov, P. Maksymovych, V. Ya. Shur, V. Gopalan, L. Q. Chen, and S. V. Kalinin, Phys. Rev. B **80**, 214110 (2009).
[44] See supplementary material at http://link.aps.org/supplemental/10.1103/PhysRevB.82.024111 for details of calculations.